Generating Ultralong-Superoscillation Nondiffracting Beams with Full Control of the Intensity Profile

Kun Zhang,[1,2] Hai Jiang,[1] Fengliang Dong,[2,3,4] Haifeng Hu,[2,3,4] Zhiwei Song,[2,3,4] Lihua Xu,[2,3,4] Zhengguo Shang,[1] Gaofeng Liang,[1] Zhihai Zhang,[1] Zhongquan Wen,[1] Yi Zhou,[1,*] Luru Dai,[2,5,†] Weiguo Chu,[2,3,4,‡] and Gang Chen[1,§]

[1] *Laboratory of Optoelectronic Technology and Systems (Chongqing University), Ministry of Education, School of Optoelectronic Engineering, Chongqing University, 174 Shazheng Street, Shapingba, Chongqing 400044, China*

[2] *National Center for Nanoscience and Technology, No.11 Zhong Guan Cun Bei Yi Tiao, Beijing 100190, China*

[3] *CAS Key Laboratory of Nanosystem and Hierarchical Fabrication, Nanofabrication Laboratory, CAS Center for Excellence in Nanoscience, National Center for Nanoscience and Technology, Beijing 100190, China*

[4] *Center of Materials Science and Optoelectronics Engineering, University of Chinese Academy of Sciences, Beijing 100049, China*

[5] *Key Laboratory of Biomedical Effects of Nanomaterials and Nanosafety, Chinese Academy of Sciences and CAS Center for Excellence in Nanoscience, National Center for Nanoscience and Technology, Beijing 100190, China*

(Received 1 September 2022; revised 9 November 2022; accepted 8 December 2022; published 13 January 2023)

Nondiffracting light beams receive substantial attention in various areas due to their properties of diffractionless propagation and achievable subwavelength beam size. Extending the propagation distance and compressing the beam size of nondiffracting beams are crucial to their practical applications. However, it remains challenging to achieve nondiffracting light beams with a subwavelength subdiffracting transverse size and a long propagation distance with controllable intensity profiles in both transverse and longitudinal directions. Here, we propose an optimization method to generate an ultralong-superoscillation nondiffracting light beam with full control of the beam intensity profile. A 45λ-long-superoscillation nondiffracting light beam, the transverse sizes of which are within the range of 0.37λ–0.4λ along the propagation axis, is experimentally demonstrated by a metalens based on continuous phase modulation using geometrical phase metasurfaces. Our method provides an attractive way to controllably generate ultralong-superoscillation nondiffracting beams on a subwavelength scale and might find fascinating applications in optical manipulation, materials processing, data storage, microscopy, and spectroscopy.

DOI: 10.1103/PhysRevApplied.19.014041

I. INTRODUCTION

The spreading of a light beam during its propagation is an inevitable result of the diffracting nature of electromagnetic waves. Since Durnin *et al.* proposed the concept of nondiffracting optical beams in 1987 [1], tremendous works have been conducted to develop various methods to realize nondiffracting beams. They include axicons [2–4], diffraction gratings [5], aberrating lenses [6], annular-type photonic crystals [7], liquid crystals [8], computer-generated holograms [9], subwavelength annular apertures [10], Fresnel zone plates [11,12], and spatial light-modulation devices [13–16]. Due to their properties of diffractionless propagation, self-healing, and high local intensity, nondiffracting beams find wide applications in optical manipulation [17], materials processing [18,19], optical imaging [20], optical microscopy [21–24], and spectroscopy [25]. However, most research is only concerned with the diffractionless property of nondiffracting beams, while little attention is paid to their transverse size. Axicons, which combine positive and negative axicons with similar refractive indexes, can generate a nondiffracting beam with a propagation distance of 200 m and spot size of 500 μm. However, it is hard to compress the corresponding focusing spot size to be on the nanometer scale because of the small diffraction angle [4]. Diffraction gratings, which can realize a propagation distance of 230 cm, can only compress the beam size to several micrometers, due to the large unit pixel size of the spatial light modulator. Aberrating lenses that can generate a nondiffracted beam by blocking the middle of the spherical lens are also unable to form a spot size on the nanometer scale [6]. For holograms, the transverse size of the generated

*yi_zhou@cqu.edu.cn
†dai@nanoctr.cn
‡wgchu@nanoctr.cn
§gchen1@cqu.edu.cn

nondiffracting beam is also on the micrometer scale. Overall, the reported transverse beam size is always greater than the working wavelength, λ. However, in the applications of nanomanipulation, nanofabrication, superresolution imaging, and nanomicroscopy, a subwavelength beam size is extremely attractive in the visible range. Achieving the subwavelength beam size requires interference from high-spatial-frequency components, which is hard to realize with conventional optics. Recently, the microsphere has become an important tool to achieve superresolution and has presented so many practical applications in both nanoimaging and nanofabrication [26,27]. However, the propagation distance of the focusing spot by a microsphere is somewhat limited to several wavelengths, due to its shallow depth of focus. Another technique of quantum photonics based on a metasurface can be used as an alternative way to produce superresolution focusing [28]. Moreover, a waveguide-metasurface-based superlens is proposed to realize a FWHM of 98 nm (λ/4.13) and a focal length of 1.49 μm (3.68λ) at a wavelength of 405 nm. Nevertheless, the working distance of the waveguide-metasurface-based superlens is very short, which is inconvenient for practical applications, such as far-field superresolution microscopy [29]. Optical superoscillation [30–35], which is smaller than the size allowed by the conventional Abbe diffraction limit [36], i.e., 0.5λ/NA, where λ is the wavelength and NA is the effective numerical aperture, provides an alternative way to create optical fields with subwavelength features. Various types of superresolution lenses are either theoretically or experimentally demonstrated for scalar optical fields [37–39] and vectorial optical fields [40–42]. Superresolution optical needles [3,43–47] with lengths of several wavelengths are reported. Based on the ideas of angular spectrum compression [48,49] and superoscillation, a superresolution nondiffracting beam is also experimentally demonstrated by specially designed Fresnel lenses for circular, azimuthal, and radial polarized light with a propagation distance of more than 70λ. Subwavelength generation of nondiffracting structured beams with a propagation distance of 16λ is achieved by utilizing the interference from the light of high-spatial-frequency wave vectors generated by being scattered on a circular shaped edge obstacle [43,50]. However, this method may have a comparatively low efficiency and largely rely on the edge quality. The inverse design method is also proposed for generating an optical needle field by reversing the electric-dipole-array radiation, which requires a spatial filter for both multilevel amplitude modulation and binary phase modulation to achieve a needle length of several wavelengths [47].

In the design of realizable subwavelength nondiffracting beams, full control of the beam profile is highly desired in both transverse and longitudinal directions. Theoretically, this can be completed by overlapping multifocusing points [51], the transverse size of which must be optimized point by point to achieve the subwavelength scale. However, the computational load tremendously increases with the propagation distance. It still remains a challenge to realize intensity-profile-controllable nondiffracting beams with subwavelength and subdiffracting transverse sizes and long propagation distances. Recent progress in optical metasurfaces [52] provides a flexible way to realize optical devices that can manipulate the optical fields in multiple dimensions at the subwavelength scale, including amplitude, phase, and polarization. Geometrical phase metasurfaces, due to their simple structure and ease of fabrication, can realize a straightforward continuous phase modulation of 0–2π by simply rotating the structure, which is favorable for generating high-spatial-frequency wave vectors to realize nondiffracting beams with subwavelength subdiffracting transverse sizes and long propagation distances. Here, we propose a forward optimization method for generating an ultralong-superoscillation nondiffracting light beam with full control of the beam intensity profile. Both numerical and experimental studies are conducted to demonstrate the validity of the proposed method.

II. PRINCIPLE OF THE METHOD

The nondiffracting beam proposed by Durnin *et al.* is a simple solution of the Helmholtz equation, the central spot radius of which can be highly narrow without being subject to diffractive spreading. The electrical field of the Durnin nondiffracting modes satisfies Eq. (1) [1], which describes a monochromatic wave propagating in the z direction. In Eq. (1), $J_0(\rho r)$ is the zero-order Bessel function, ρ is the radial component of the in-plane wave vector, r is the radial coordinate, and k_z is the z component of the wave vector. The physical explanation for the formation of the nondiffracting beam is the interference of plane waves with wave vectors lying on the surface of a cone with a coning angle of $2\theta_c$. With a given wave vector $k = 2\pi/\lambda$, we have $\rho = k\sin\theta_c$ and $k_z = k\cos\theta_c$.

$$E(r,z) = J_0(\rho r)\exp(j k_z z). \tag{1}$$

The transverse size of the beam is determined by the first zero of the zero-order Bessel function, i.e., $r_0 = 2.4048/\rho$, indicating the fact that the beam size decreases as ρ increases, and the theoretical minimum beam size is approximately 0.383λ. However, Durnin's solutions are accurate in infinite free space, whereas the generation of such beams requires an infinite aperture. Such an infinite aperture is not applicable for practical realization. In the practical realization, a finite aperture always results in a strong intensity variation along the propagation axis in the demonstrated nondiffracting beams.

An optical device for generating a nondiffracting beam can be realized by applying a linear phase profile along the radial axis, according to its physical explanation, as expressed in Eq. (2). Figure 1 shows a typical nondiffracting beam produced by a conventional axicon, the phase

profile of which can be described by Eq. (2), where λ is the wavelength and θ_c corresponds to the angle of the wave vector after the axicon. As shown in Figs. 1(b) and 1(c), the longitudinal optical profile shows an apparent fluctuation and a clearly increasing trend during propagation.

$$\phi(r) = \left(-\frac{2\pi}{\lambda}\sin\theta_c\right) r. \tag{2}$$

According to the Rayleigh-Sommerfeld diffraction theory [53], for any given transmission function of $t(r)$, the diffraction pattern on the optical axis can be described by the longitudinal Rayleigh-Sommerfeld method (LRSM), as given in Eq. (3). The method can be used to simply obtain the optical intensity on the optical axis from a one-dimensional integral.

$$E(z) = \int_0^R t(r)\frac{\exp(jkL)}{L}\frac{z}{L}\left(-jk + \frac{1}{L}\right) r dr, \tag{3}$$

where $t(r)$ is the transmission function of the lens at $z = 0$, R is the radius of lens, and $L = \sqrt{r^2 + z^2}$.

The diffraction pattern on the transverse plane at any given position z can be obtained by the transverse angular spectrum method (TASM), as given in Eq. (4). This method can be further simplified for different polarizations under circular symmetrical cases [54].

$$\begin{aligned} E(r,z) &= \int_{-\infty}^{\infty}\int_{-\infty}^{\infty} [T(k_x,k_y)\exp(j\,k_z z)] \\ &\quad \times \exp[j\,(k_x x + k_y y)] dk_x dk_y, \\ T(k_x,k_y) &= \int_{-\infty}^{\infty}\int_{-\infty}^{\infty} t(x,y,z=0) \\ &\quad \times \exp[-j\,(k_x x + k_y y)] dx dy. \end{aligned} \tag{4}$$

To fully control both the transverse and on-axis intensity profiles, we can add one additional phase profile, $\varphi(r)$, to the phase profile described in Eq. (2), and the final phase profile of the target lens can be expressed by Eq. (5), where $A(r)$ is a radial-coordinate-dependent additional parameter that is much smaller than $\sin\theta_c$. For any given additional phase $\varphi(r)$, the intensity profile on the optical axis, $I_z(z)$, and the intensity profile on the transverse cross section, $I_{xy}(r, z_0)$, at z within the beam-propagation range can be directly calculated using Eqs. (3) and (4), respectively. Utilizing the spreadingless property of nondiffracting beams, we can obtain information on the transverse intensity profile, such as the full width at half maximum (FWHM) and the sidelobe ratio (SR, the ratio of maximum sidelobe intensity to the central lobe intensity) based on the diffraction pattern on the vertical plane at any point within the propagation range. In the present case, the midpoint of the beam, $z = z_m$, is chosen for calculating the transverse intensity profile.

$$\begin{aligned} \psi(r) &= -\frac{2\pi}{\lambda} r\sin\theta_c + \varphi(r), \\ \varphi(r) &= -\frac{2\pi}{\lambda} r A(r). \end{aligned} \tag{5}$$

Therefore, to obtain information on the transverse and longitudinal intensity profiles, we need only to calculate two integrals, i.e., Eqs. (3) and (4). Figure 2(a) gives the major longitudinal parameters of a nondiffracting beam, including the mid position of the nondiffracting beam, Z_m; the propagation distance, D; the on-axis maximum intensity, $I_{\max}$, and minimum intensity, $I_{\min}$; and the on-axis intensity fluctuation, $\delta I = (I_{\max} - I_{\min})/I_{\max}$. Figure 2(b) gives the major transverse parameters of the nondiffracting beam, including the transverse-size FWHM and the sidelobe ratio (the ratio of the maximum sidelobe intensity to the central lobe intensity). As shown in Fig. 2(c), for given target parameters, i.e., working wavelength λ, beam middle position Z_m, propagation distance D_{target}, on-axis intensity fluctuation δI_{target}, transverse-size $\text{FWHM}_{\text{target}}$, and sidelobe ratio S_{target}, the additional phase distribution $\varphi(r)$ can be optimized using optimization methods, such as the particle-swarm algorithm [55] and gene algorithm [56], with the procedure presented in Fig. 2(c). The optimization iteration continues until the results meet the all requirements of the target parameters.

III. SIMULATION, EXPERIMENTS, AND RESULTS

To verify the proposed approach, a metalens with radius $R_{\text{lens}} = 300\lambda$ and NA of 0.9 is optimized to create a superoscillation nondiffracting beam under the illumination of collimated circularly polarized light at a wavelength of $\lambda = 405$ nm. The beam middle point, Z_m, is 112λ; the target working distance, W_{target}, is 89λ; the target propagation distance is $D_{\text{target}} = 45\lambda$; the target intensity fluctuation, δI_{target}, is smaller than 20%; at the middle point of the beam, Z_m, the target transverse-beam-size $\text{FWHM}_{\text{target}}$ is smaller than 0.4λ; and the target sidelobe ratio, S_{target}, is smaller than 20%. In our design, the lens is divided into N ring-belt areas with the same width of $P = 0.494\lambda$, and the additional phase $\varphi(r_i)$ is optimized for each of the ring belt, where $r_i = iP$ and $i = 1, 2, \ldots, N$. The central part of the lens, which is used to control the working distance of the lens, has a uniform phase of 0 within the area of $r < R_b$ ($R_b = 160\lambda$).

A. Simulation results

To compare the differences between a conventional axicon and our proposed metalens, both phase profiles are presented in Fig. 3. Figure 3(a) gives the phase profile

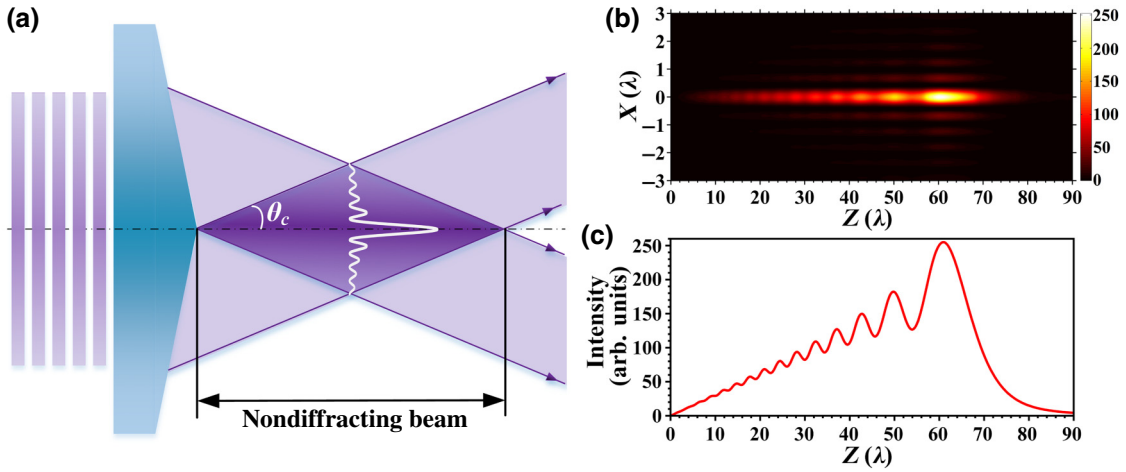

FIG. 1. Nondiffracting beam generated by using a conventional axicon. (a) Schematic of producing a nondiffracting beam with a conventional axicon. (b) Intensity distribution of the nondiffracting beam generated by a conventional axicon with a phase profile described by Eq. (2), where $R = 150\lambda$ and $\sin\theta_c = 0.9$. (c) Axial optical profile of the generated nondiffracting beam, showing a clear fluctuation and increasing trend as the beam propagates forward.

of a conventional axicon (left) and the angular spectra (right) of the conventional axicon (top) and an axicon metalens (bottom) with the same parameters of $R_{\text{lens}} = 300\lambda$, $R_b = 160\lambda$, and NA = 0.9. The conventional axicon has a continuous spatial phase distribution along the radial direction. The axicon metalens is divided into N ring-belt areas with the same width of $P = 0.494\lambda$, in which the phase is determined by $-2\pi\lambda\sin\theta_c r_i$. It is found that the angular spectrum of the conventional axicon has a narrow peak at $0.9f_c$, where f_c is the cutoff spatial frequency of the wave, i.e., $f_c = 1/\lambda$. However, the angular spectrum of the axicon metalens shows additional peaks at lower frequency, especially the enhanced zero-frequency component, which is even greater than the amplitude of the peak at $0.9f_c$. This is attributed to the discrete phase distribution of the axicon metalens. Figure 3(b) illustrates the phase profile (left) and angular spectrum (right) of the optimized lens, where 16 different discrete phase values with equal intervals are

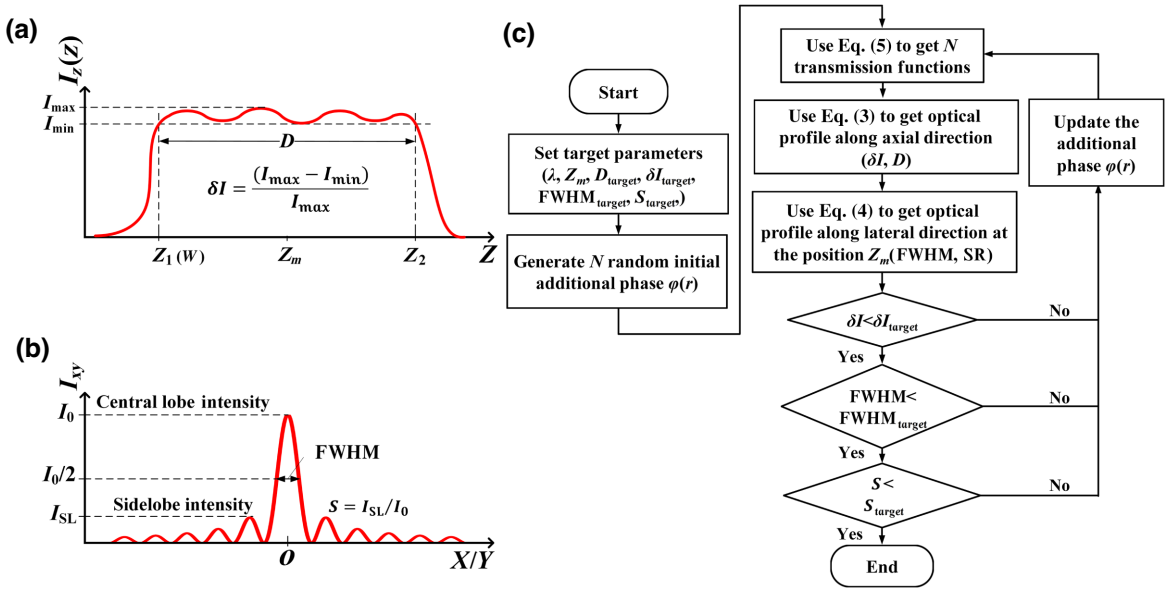

FIG. 2. (a) Definition of the longitudinal parameters of a nondiffracting beam, including the middle position of the nondiffracting beam, Z_m; the propagation distance, D; the on-axis maximum intensity, $I_{\max}$, and minimum intensity, $I_{\min}$; and the on-axis intensity fluctuation, $\delta I = (I_{\max} - I_{\min})/I_{\max}$. (b) Definition of the transverse parameters of a nondiffracting beam, including the transverse-size FWHM and the sidelobe ratio (the ratio of the maximum sidelobe intensity to the central lobe intensity). (c) Flow chart of the optimization procedure for the nondiffracting beam.

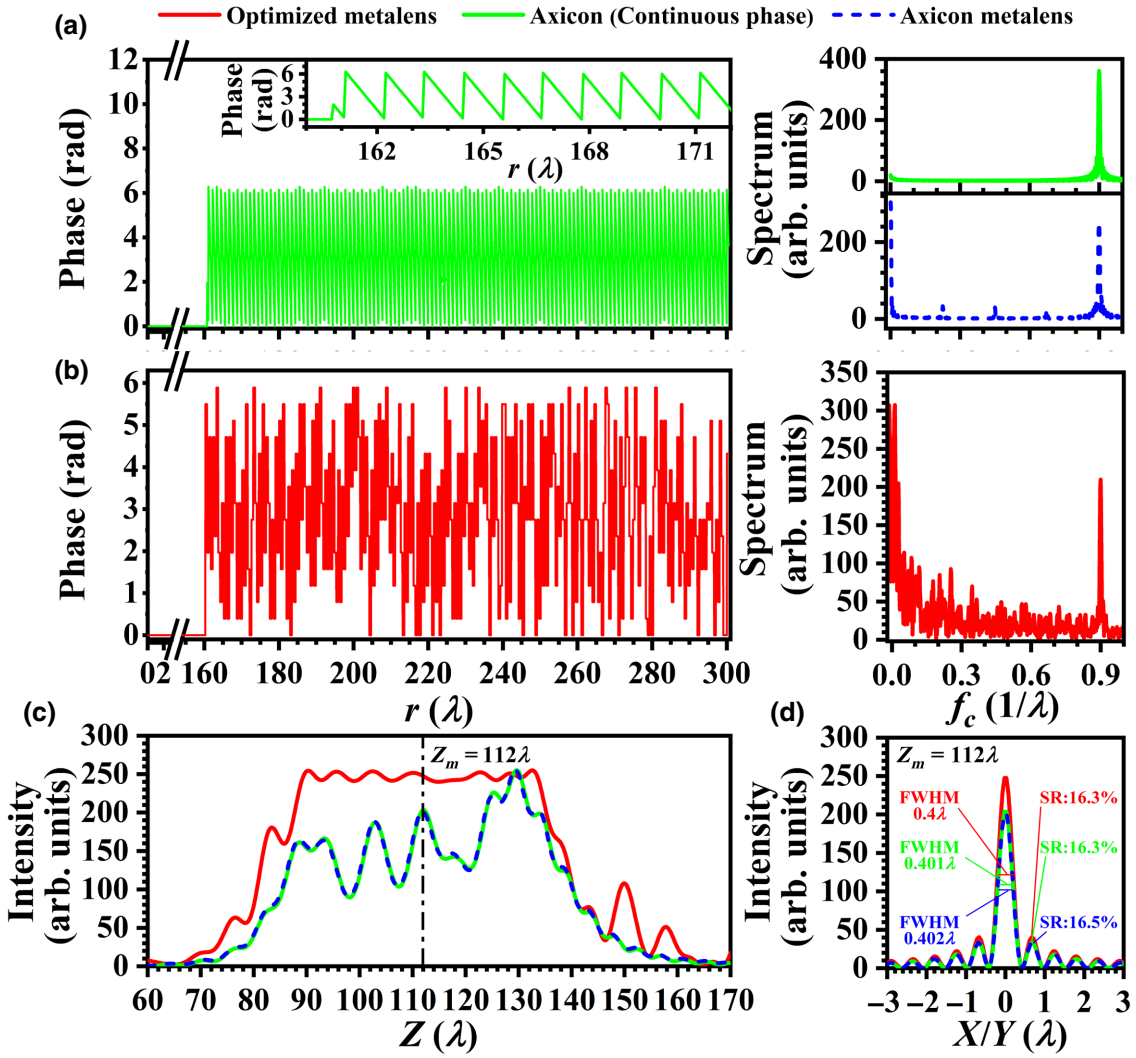

FIG. 3. Optimized metalens and its predicted performance. (a) Phase profile (left) of a conventional axicon described by Eq. (2) with $R_{\text{lens}} = 300\lambda$, $R_b = 160\lambda$, and NA = 0.9; and corresponding angular spectrum of the axicon (right), where the result of the conventional axicon is presented in green and the result of the axicon metalens is plotted in blue. (b) Phase profile (left) of the optimized lens using the proposed method with the same parameters of $R_{\text{lens}} = 300\lambda$, $R_b = 160\lambda$, and NA = 0.9; and corresponding angular spectrum of the optimized lens (right). (c) Longitudinal optical intensity profile of the optimized nondiffracting beam (red), where the result of the conventional axicon is presented in green and the result of the axicon metalens is plotted in blue. (d) Transverse optical intensity profile (red) of the beam at the location of $Z_m = 112\lambda$, where the result of the conventional axicon is presented in green and the result of the axicon metalens is plotted in blue.

adopted in the optimization. Obviously, the phase profile shows little similarity to that of the conventional axicon. However, the proposed lens also shows a strong spatial frequency component (narrow spatial frequency band) at $0.9f_c$, corresponding to a numerical aperture of NA = 0.9. This proves that, although the designed phase profile is different from the conventional axicon, the proposed lens does generate nondiffraction, as indicated by the strong spatial frequency component (narrow spatial frequency band) at $0.9f_c$. Similar to the axicon metalens, the proposed lens also has a strong zero-frequency component due to the discrete phase distribution. Meanwhile, unlike the conventional axicon and the axicon metalens, the proposed lens has nonzero frequency components over the whole frequency band below the cutoff frequency, which play an important role in reducing the intensity fluctuation along the optical axis within the beam-propagation range.

The longitudinal optical intensity profile (red) of the optimized nondiffracting beam is presented in Fig. 3(c), showing a small intensity variation of 7.05% between $z = 89\lambda$ and $z = 134\lambda$ on the optical axis. The longitudinal optical intensity profiles are also plotted for the conventional axicon (green) and the axicon metalens (blue), which show the same intensity distributions with strong

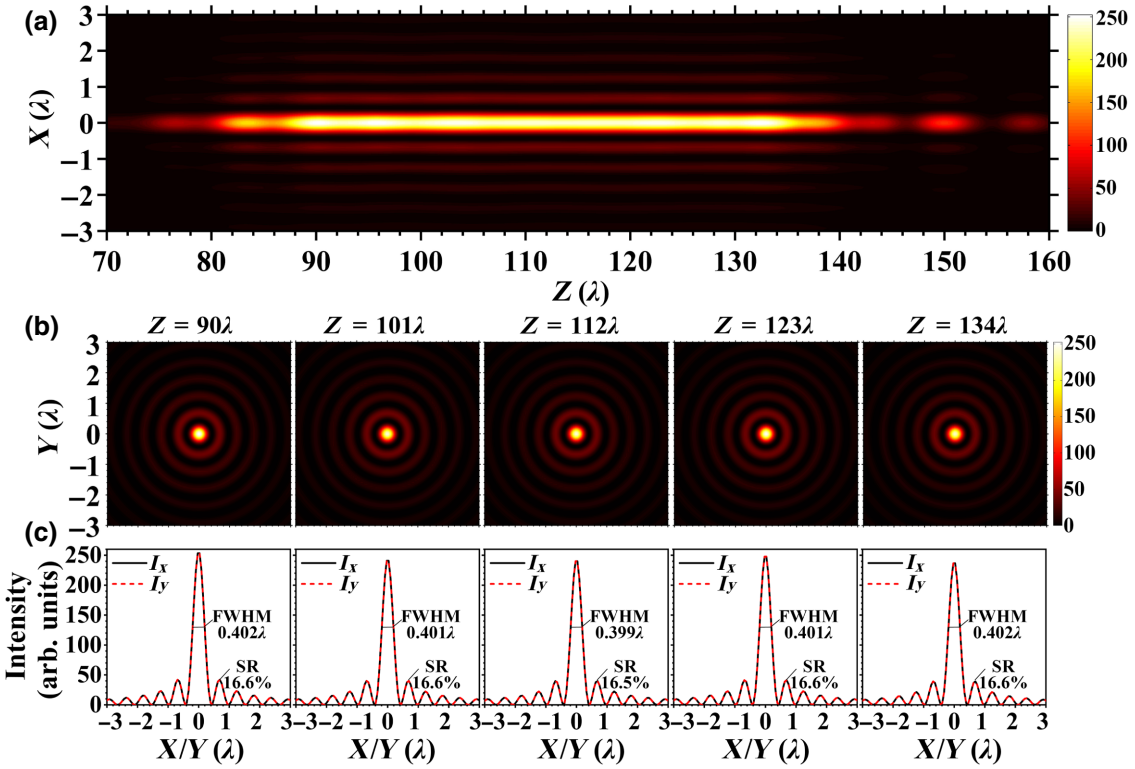

FIG. 4. Simulation results of the intensity profile of the generated nondiffracting beam obtained by TASM. (a) Calculated optical intensity distribution on the X-Z propagation plane. (b) Two-dimensional transverse optical intensity distributions on the X-Y plane at different propagation positions of 90λ, 101λ, 112λ, 123λ, and 134λ. (c) Corresponding transverse optical intensity profiles along the x axis (black) and y axis (red).

fluctuation along the optical axis within the spatial range of concern. Figure 3(d) illustrates the transverse optical intensity profile (red) of the beam at a location of $Z_m = 112\lambda$, showing a FWHM and SR of 0.399λ and 16.5%, respectively. For comparison, the on-axis optical intensity profiles are also plotted in Fig. 3(d) to illustrate the results of the conventional axicon (green) and the axicon metalens (blue), showing a strong fluctuation in intensity along the optical axis. The FWHM is 0.401λ and the SR is 16.3% at the middle point of the nondiffracting beam generated by the conventional axicon, and the FWHM is 0.402λ and the SR is 16.5% at the middle point of the nondiffracting beam generated by the axicon metalens. Both the conventional axicon and the axicon metalens show excellent agreement with the corresponding results of our designed lens in the transverse field distribution at $Z = Z_m$. This again indicates the advantages of our superoscillation nondiffracting beam, that is, the beam intensity fluctuation is effectively reduced, while its transverse properties remain almost unchanged.

To quantitatively illustrate the performance of the proposed nondiffracting-beam metalens, Fig. 4 presents the simulation results of the generated nondiffracting beam obtained by TASM. The intensity distribution on the X-Z propagation plane shows a noticeable narrow beam between $z = 89\lambda$ and $z = 134\lambda$. The surrounding sidelobes are comparatively weak. Figure 4(b) depicts the transverse intensity distribution at different points on the beam at $z = 90\lambda$, 101λ, 112λ, 123λ, and 134λ. The corresponding intensity distribution curves on the x axis (black) and y axis (red) are plotted in Fig. 4(c). The FWHMs of the focusing spots are calculated to be 0.402λ, 0.401λ, 0.399λ, 0.401λ, and 0.402λ, respectively. All simulated spot sizes are equal to or smaller than the superoscillation criterion ($0.38\lambda/\mathrm{NA} = 0.42\lambda$), showing the capability of forming a superoscillation nondiffracting beam along a long propagation distance. The sidelobe ratios are 16.6%, 16.6%, 16.5%, 16.6%, and 16.6%, respectively, for these different locations along the optical axis. It is noted that the FWHM and SR show little variation at these different locations, showing the diffractionless property of the generated beam and validity of our proposed method.

Moreover, detailed information on the peak intensity, FWHM, and SR along the optical axis within the propagation distance are plotted in Fig. 5, where the diffraction limit ($0.5\lambda/\mathrm{NA}$) and superoscillation criteria ($0.38\lambda/\mathrm{NA}$) are plotted as black and wine-colored dotted-dashed lines, respectively. The longitudinal optical intensities obtained by LRSM show good agreement with the results obtained by TASM, by which the diffraction pattern is calculated point by point along the optical axis. The intensity

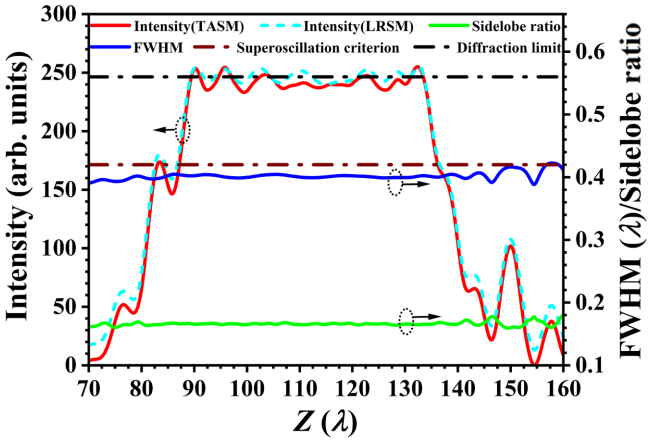

FIG. 5. Major parameters of the optimized nondiffracting beam between $z = 70\lambda$ and $z = 160\lambda$ obtained by numerical simulation. Cyan dashed curve presents the longitudinal optical intensities obtained with LRSM; red curve shows the longitudinal optical intensities obtained by point-by-point diffraction-pattern calculations with TASM; blue and green curves illustrate the FWHM and sidelobe ratio, respectively. Black and wine-colored dashed-dotted lines denote the diffraction limit (i.e., $0.5\lambda/\mathrm{NA} = 0.56\lambda$) and superoscillation criterion (i.e., $0.38\lambda/\mathrm{NA} = 0.42\lambda$) for the lens with NA = 0.9, respectively.

shows a small fluctuation within the beam-propagation distance, which is calculated to be approximately 12.5%. It is also seen that the FWHM and SR remain almost unchanged over the entire beam range. The FWHM varies over a small range between 0.399λ and 0.404λ, and the SR varies between 16.4% and 16.8% in the beam region between $z = 89\lambda$ and $z = 134\lambda$. It is seen that the transverse size of the nondiffracting beam has superresolution and is superoscillatory over the entire propagation distance.

B. Lens fabrication

To fabricate the designed lens, a TiO_2 cubic-block-based meta-atom is optimized to realize the desired phase profile. Figure 6(a) presents the structure of the TiO_2 cubic block on the top surface of a SiO_2 glass plate. The unit size of the meta-atom is $P = 0.494\lambda$ (200 nm). The length, width, and height of the cubic block are $L_x = 145$ nm, $L_y = 75$ nm, and $H = 560$ nm, respectively. The refractive indexes are 1.47 and 2.497 for the SiO_2 plate and TiO_2, respectively, at a wavelength of $\lambda = 405$ nm. The amplitude transmission rate of this meta-atom is approximately 92%, with little variation in the rotation angle. As shown in Fig. 6(b), the metalens is divided into a series of concentric ring belts with a width of P, and the central position of each meta-atom is represented by r_i, where i represents the numbering of the ring belt. According to the property of geometrical phase, the meta-atom rotation angle, β_i, at r_i is equal to $\Psi(r_i)/2$.

A 500-μm-thick SiO_2 plate is first cleaned with traditional piranha solution (a 3:1 mixture of sulfuric acid and 30% hydrogen peroxide) and acetone. We use the magnetron sputtering method (Endeavor AT500, Magnetron *S*-gun sputtering system) to deposit a 560-nm-thick TiO_2 layer on the front side of the SiO_2 substrate. Then we grow a 78-nm-thick chromium-film hard mask on both sides of the device. The pattern of the metalens is transferred to the hard mask using *e*-beam lithography (Vistec EBPG 5000plus ES, Vistec Electron Beam GmbH). Finally, the metalens is developed using inductively coupled plasma

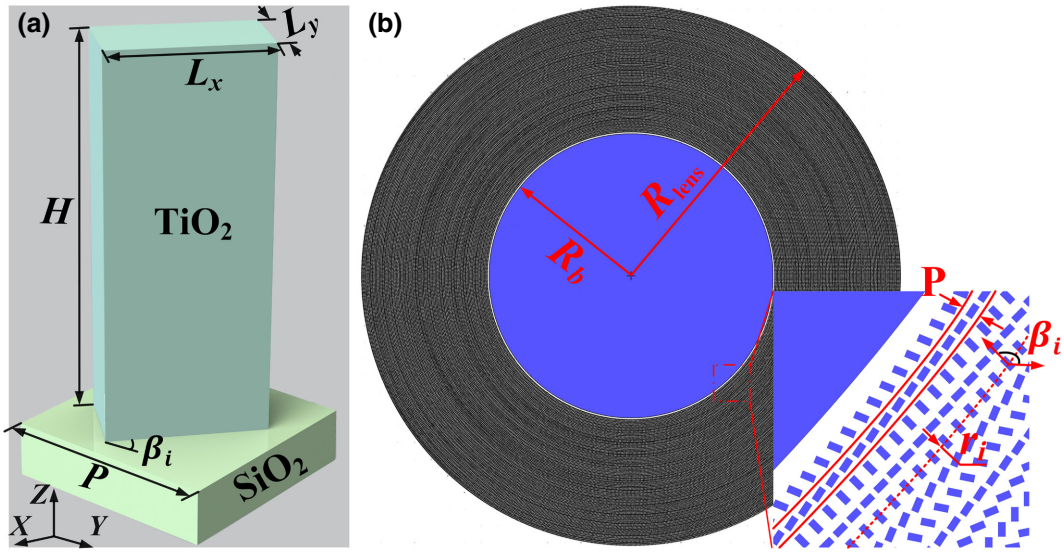

FIG. 6. Nondiffracting superoscillation metalens based on TiO_2 metasurfaces. (a) TiO_2 geometric phase meta-atom for continuous phase modulation. (b) Diagram of the meta-atom arrangement on the proposed metalens; inset shows the details of several ring belts.

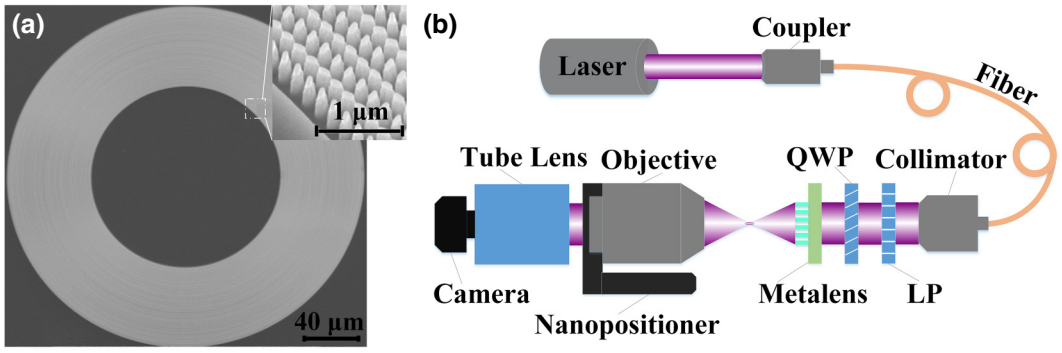

FIG. 7. Fabricated metalens and experimental schematic. (a) Scanning-electron-microscope image of the fabricated metalens. (b) Experimental setup to obtain the optical intensity distribution of the proposed metalens, where LP represents linear polarizer.

etching (Sentech PTSA SI 500, SENTECH Instruments GmbH).

C. Experimental results

A scanning-electron-microscope image of the fabricated metalens is presented in Fig. 7(a). The experimental setup for the characterization of the metalens is depicted in Fig. 7(b). A laser beam at a wavelength of 405 nm (MDL-C-405-50 mW, Changchun New Industries Optoelectronics Tech. Co. Ltd.) is used as the illumination source ; the laser beam is first coupled into a single-mode fiber (P1-405B-FC-2, Thorlabs Inc.) by a coupler (F671FC-405, Thorlabs Inc.); then it is collimated by another collimator (PAF2P-A10A, Thorlabs Inc.) A quarter-wave plate (QWP, WPQ05ME-405, Thorlabs, Inc.) and a linear polarizer (WP25M-UB, Thorlabs, Inc.) are employed to convert the linearly polarized light into circularly polarized light; the laser beam normally impinges on the metalens. The optical intensity distribution generated by the metalens is finally acquired by a high-NA optical microscope.

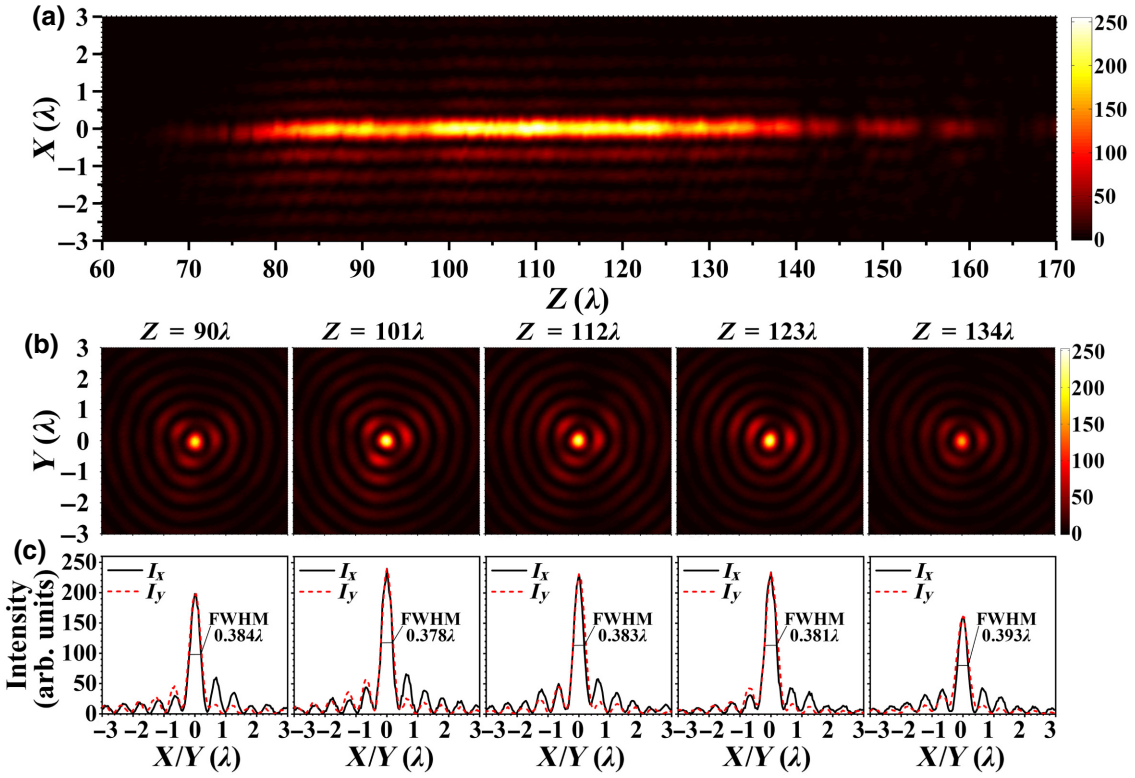

FIG. 8. Experimental results of the generated nondiffracting beam using the proposed metalens. (a) Optical intensity distribution on the X-Z propagation plane. (b) Two-dimensional transverse optical intensity distributions on the X-Y plane at different propagation distances of 90λ, 101λ, 112λ, 123λ, and 134λ. (c) Corresponding transverse optical intensities along the x axis (black) and y axis (red).

The microscope consists of an infinite objective lens (CF Plan 150×/0.95, Nikon), a one-dimensional nanopositioner (EO-S1047, Edmund Optics), a tube lens (ITL200, Thorlabs, Inc.), and a high-resolution digital camera (acA1920-25gm, Basler, Inc.) The three-dimensional optical intensity distribution can be obtained by scanning the objective along the optical axis. More details of the experimental procedure and data processing are given in S1 within the Supplemental Material [57].

Figure 8 presents the experimental results of the generated nondiffracting beam. The optical intensity distribution on the propagation plane is depicted in Fig. 8(a), which shows a clear nondiffracting beam with a propagation distance of approximately 45λ. Figure 8(b) depicts the in-plane intensity distribution at different points on the beam at $z = 90\lambda$, 101λ, 112λ, 123λ, and 134λ, and the corresponding intensity distribution curves on the x axis and y axis are plotted in Fig. 8(c). According to the experimental results, the intensity distribution shows a major central lobe surrounded by several weak sidelobes in the transverse plane for all tested cases. The major transverse parameters, i.e., FWHM and SR, are obtained by averaging the corresponding values measured at 10 different directions with equal angular intervals (0°, 18°, 36°,..., and 162°) with respect to the x axis. The average FWHMs of the focusing spots are calculated to be 0.384λ, 0.378λ, 0.383λ, 0.381λ, and 0.393λ at positions of $z = 90\lambda$, 101λ, 112λ, 123λ, and 134λ, respectively, which shows excellent agreement with their predicted values between 0.399λ and 0.404λ. The obtained spot sizes are below the superoscillation criterion (0.42λ), indicating the capability of developing a superoscillation nondiffracting beam with a long propagation distance. The average SRs are 15.9%, 18.6%, 16.3%, 17.1%, and 19.9% at these positions, respectively, which are slightly higher than the predicted value of 16%. This small deviation is believed to be caused by fabrication errors and wave-front errors in the incident illumination beam. Generally, it is noted that both the spot size and SR correspond with our theoretical design.

The traditional optical microscopic system is a linear time-invariant system, the resolution of which is limited by the diffraction limit of 0.5λ/NA. The cutoff frequency of an optical microscopic system can be indicated as nNA/λ, where n is the refractive index of the propagation medium (when the propagation medium is air, $n = 1$). The proposed metalens is a type of diffractive lens, the cutoff frequency of which is n/λ. Optical superoscillation refers to the coherent superposition of light fields with lower spatial frequencies to form a local rapid oscillating light field in the far field [58]. It is a phenomenon in which a band-limited function can contain local oscillations that are faster than those of the fastest Fourier components. In this case, the frequency components of the superoscillation focusing spot are actually smaller than the theoretical propagation cutoff frequency, i.e., although the superoscillation spot is smaller than the diffraction limit, the frequency components of the spot can still be collected by the microscope system [54,59,60]. Additionally, we conduct a

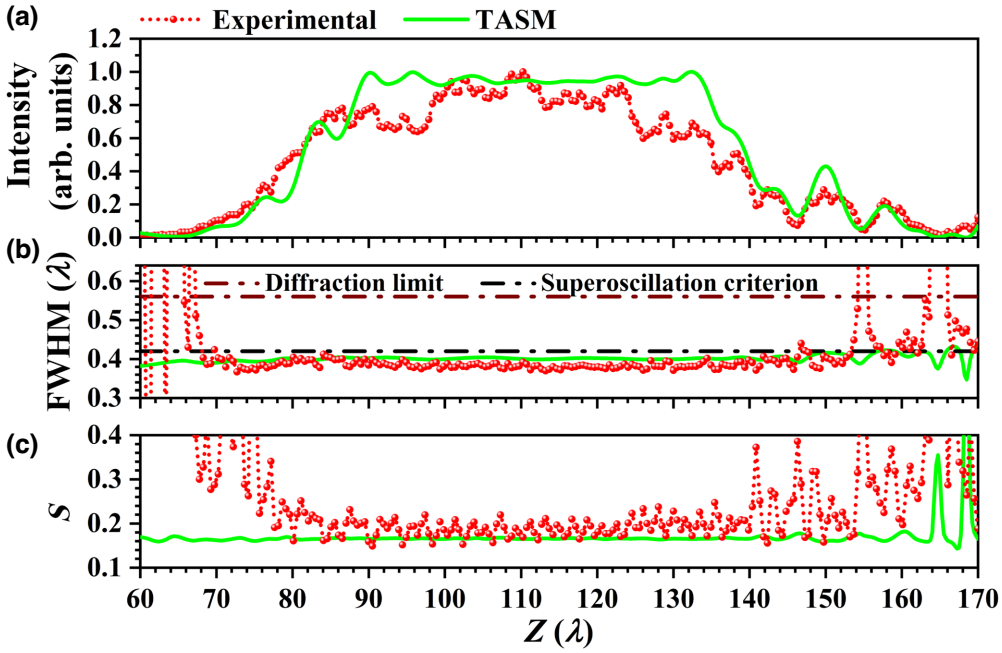

FIG. 9. Experimental (red spheres) and simulated (green line) results of (a) central lobe peak intensity; (b) beam transverse size of the FWHM, where wine-colored and black dashed-dotted lines correspond to the Abbe diffraction limit and superoscillation criterion; and (c) sidelobe ratio within the propagation range from 60λ to 170λ along the optical axis.

numerical simulation to obtain the focusing performance of the superoscillation nondiffracting beam with and without a filter effect of 0.95/λ; more details are given in S2 within the Supplemental Material [57].

To give detailed information on the entire nondiffracting beam, Figs. 9(a)–9(c) plot the experimentally (red spheres) obtained longitudinal intensity profiles, FWHM, and SR along the optical axis, respectively, where the numerical simulation results (green curves) obtained by TASM are also presented for comparison. As presented in Fig. 9(a), the intensity fluctuation is calculated to be about 27% within the propagation distance 89λ–134λ. According to the results presented in Figs. 9(b) and 9(c), the experimental results of the FWHM and SR are within the range of 0.37λ–0.4λ and 14.9%–23.7%, respectively. It is noted that the intensity fluctuation is higher than that obtained by theoretical prediction, the transverse size is slightly smaller than that of the numerical simulation, and the sidelobe ratio is slightly higher than that of the numerical result. As pointed out above, the deviation is believed to be caused by both fabrication errors and wave-front errors of the incident illumination beam. In the design, the incident beam is assumed to be a perfect plane wave, which is obviously different from that in a real case. In Fig. 9(b), the diffraction limit refers to the Abbe diffraction limit, the value of which is 0.5λ/NA [36]. In this work, the NA of our proposed superoscillation lens is 0.9. Correspondingly, the Abbe diffraction limit should be 0.56λ (0.5λ/0.9). More details on the calculation of the diffraction limit are provided in S3 within the Supplemental Material [57].

IV. CONCLUSIONS

We propose an optimization method for generating an ultralong-superoscillation nondiffracting light beam with full control of the beam intensity profile. A metalens with a pure-phase profile is optimized to generate a superoscillation nondiffracting beam with a transverse size of 0.399λ–0.404λ, a sidelobe ratio of 16.4%–16.8%, and an extremely long propagation distance of 45λ at a wavelength of $\lambda = 405$ nm. Based on continuous phase modulation, the designed TiO_2 geometrical phase metalens is fabricated. At the design wavelength of $\lambda = 405$ nm, simulated conversion efficiencies of TiO_2 meta-atoms are larger than 90%, and the focusing efficiency of our metalens is about 0.45% at a propagation distance of 112λ. The focusing efficiency of most of the existing methods is about 0.1% [2–4,6,13–16], while our method can improve the efficiency up to about 0.45%. Experiments are conducted to verify the focusing performance of the proposed metalens. The experimental results show that the intensity fluctuation is calculated to be about 27% within a propagation distance of 45λ. The FWHM and SR are within the ranges of 0.37λ–0.4λ and 14.9%–23.7%, respectively. Consequently, the experimental and simulated results are in good agreement, achieving a superoscillation nondiffracting beam with full control of both longitudinal and transverse intensity profiles. Our method provides an attractive way to generate an ultralong superresolution nondiffracting beam at the subwavelength scale through simple calculations.

There are many applications of a superoscillation nondiffracting beam, such as in nanomanipulation, nanofabrication, superresolution imaging, and nanomicroscopy. For example, superoscillation nondiffracting beams can be applied to unlabeled superresolution microscopic systems. Hong and co-workers [61] proposed a supercritical optical needle with a transverse size of 0.407λ and a focal depth of 12λ at a wavelength of 405 nm. Applying the supercritical lens in a confocal microscopy system, they successfully visualized two circular holes with a diameter of 165 nm and a spacing of 65 nm. Another advantage of their supercritical optical needle microscopy is the capability of mapping the horizontal details of a three-dimensional object in one go. Besides superresolution microscopic systems, a superoscillation nondiffracting light beam has the potential to be used to fabricate nanostructures with great uniformity of depth.

ACKNOWLEDGMENTS

This work has received funding from the National Natural Science Foundation of China (Project No. 61927818). The authors would like to extend their sincere thanks to Professor Jiang Ting and Professor Zou Yuanpeng at the School of Foreign Languages and Cultures, Chongqing University, for their assistance in language polishing.

[1] J. Durnin, J. Miceli, Jr, and J. H. Eberly, Diffraction-Free Beams, Phys. Rev. Lett. **58**, 1499 (1987).
[2] J. H. McLeod, The axicon: A new type of optical element, J. Opt. Soc. Am. A **44**, 592 (1954).
[3] L. Turquet, X. Zang, J. P. Kakko, H. Lipsanen, G. Bautista, and M. Kauranen, Demonstration of longitudinally polarized optical needles, Opt. Express **26**, 27572 (2018).
[4] N. Zhang, J. S. Ye, S. F. Feng, X. K. Wang, P. Han, W. F. Sun, Y. Zhang, and X. C. Zhang, Generation of long-distance stably propagating Bessel beams, OSA Continuum **4**, 1223 (2021).
[5] P. García-Martínez, M. M. Sánchez-López, J. A. Davis, D. M. Cottrell, D. Sand, and I. Moreno, Generation of Bessel beam arrays through Dammann gratings, Appl. Opt. **51**, 1375 (2012).
[6] R. Herman and T. Wiggins, Production and uses of diffractionless beams, J. Opt. Soc. Am. A **8**, 932 (1991).
[7] H. Kurt and M. Turduev, Generation of a two-dimensional limited-diffraction beam with self-healing ability by annular-type photonic crystals, J. Opt. Soc. Am. B **29**, 1245 (2012).

[8] A. Hakola, A. Shevchenko, S. C. Buchter, M. Kaivola, and N. V. Tabiryan, Creation of a narrow Bessel-like laser beam using a nematic liquid crystal, J. Opt. Soc. Am. B **23**, 637 (2006).

[9] N. Davidson, A. Friesem, and E. Hasman, Holographic axilens: High resolution and long focal depth, Opt. Lett. **16**, 523 (1991).

[10] Y.-Y. Yu, D. Z. Lin, L. S. Huang, and C. K. Lee, Effect of subwavelength annular aperture diameter on the non-diffracting region of generated Bessel beams, Opt. Express **17**, 2707 (2009).

[11] A. Sabatyan and B. Meshginqalam, Generation of annular beam by a novel class of Fresnel zone plate, Appl. Opt. **53**, 5995 (2014).

[12] A. Vijayakumar and S. Bhattacharya, Phase-shifted Fresnel axicon, Opt. Lett. **37**, 1980 (2012).

[13] L. Gong, Y. X. Ren, G. S. Xue, Q. C. Wang, J. H. Zhou, M. C. Zhong, Z. Q. Wang, and Y. M. Li, Generation of non-diffracting Bessel beam using digital micromirror device, Appl. Opt. **52**, 4566 (2013).

[14] K. G. Makris and D. Psaltis, Superoscillatory diffraction-free beams, Opt. Lett. **36**, 4335 (2011).

[15] E. Greenfield, R. Schley, I. Hurwitz, J. Nemirovsky, K. G. Makris, and M. Segev, Experimental generation of arbitrarily shaped diffractionless superoscillatory optical beams, Opt. Express **21**, 13425 (2013).

[16] J. Wu, Z. Wu, Y. He, A. Yu, Z. Zhang, Z. Wen, and G. Chen, Creating a nondiffracting beam with sub-diffraction size by a phase spatial light modulator, Opt. Express **25**, 6274 (2017).

[17] M. Dienerowitz, M. Mazilu, and K. Dholakia, Optical manipulation of nanoparticles: A review, J. Nanophotonics **2**, 021875 (2008).

[18] M. Duocastella and C. B. Arnold, Bessel and annular beams for materials processing, Laser Photonics Rev. **6**, 607 (2012).

[19] H. Wang, F. Zhang, and K. Ding, Non-diffraction-length Bessel-beam femtosecond laser drilling of high-aspect-ratio microholes in PMMA, Optik **229**, 166295 (2021).

[20] N. Weber, D. Spether, A. Seifert, and H. Zappe, Highly compact imaging using Bessel beams generated by ultra-miniaturized multi-micro-axicon systems, J. Opt. Soc. Am. A **29**, 808 (2012).

[21] G. Thériault, Y. De Koninck, and N. McCarthy, Extended depth of field microscopy for rapid volumetric two-photon imaging, Opt. Express **21**, 10095 (2013).

[22] W. Yu, Z. Ji, D. Dong, X. Yang, Y. Xiao, Q. Gong, P. Xi, and K. Shi, Super-resolution deep imaging with hollow Bessel beam STED microscopy, Laser Photonics Rev. **10**, 147 (2016).

[23] F. O. Fahrbach, P. Simon, and A. Rohrbach, Microscopy with self-reconstructing beams, Nat. Photonics **4**, 780 (2010).

[24] V. Ebrahimi, J. Tang, and K. Y. Han, Incoherent superposition of polychromatic light enables single-shot non-diffracting light-sheet microscopy, Opt. Express **29**, 32691 (2021).

[25] S. Klewitz, P. Leiderer, S. Herminghaus, and S. Sogomonian, Tunable stimulated Raman scattering by pumping with Bessel beams, Opt. Lett. **21**, 248 (1996).

[26] L. W. Chen, Y. Zhou, M. X. Wu, and M. H. Hong, Remote-mode microsphere nano-imaging: New boundaries for optical microscopes, Opto-Electron. Adv. **1**, 170001 (2018).

[27] L. W. Chen, Y. Zhou, Y. Li, and M. H. Hong, Microsphere enhanced optical imaging and patterning: From physics to applications, Appl. Phys. Rev. **6**, 021304 (2019).

[28] J. Liu, M. Q. Shi, Z. Chen, S. M. Wang, Z. L. Wang, and S. N. Zhu, Quantum photonics based on metasurfaces, Opto-Electron. Adv. **4**, 200092 (2021).

[29] Y. C. Zhu, X. L. Chen, W. Z. Yuan, Z. Q. Chu, K. Y. Wong, D. Y. Lei, and Y. T. Yu, A waveguide metasurface based quasi-far-field transverse-electric superlens, Opto-Electron. Adv. **4**, 210013 (2021).

[30] E. T. Rogers and N. I. Zheludev, Optical super-oscillations: Sub-wavelength light focusing and super-resolution imaging, J. Opt. **15**, 094008 (2013).

[31] G. Chen, Z. Q. Wen, and Z. X. Wu, Optical super-oscillation and super-oscillatory optical devices, Acta Phys. Sin. **66**, 144205 (2017).

[32] M. Berry, N. Zheludev, Y. Aharonov, F. Colombo, I. Sabadini, D. C. Struppa, J. Tollaksen, E. T. Rogers, F. Qin, and M. Hong, Roadmap on superoscillations, J. Opt. **21**, 053002 (2019).

[33] G. Chen, Z. Q. Wen, and C. W. Qiu, Superoscillation: From physics to optical applications, Light: Sci. Appl. **8**, 1 (2019).

[34] K. S. Rogers and E. T. Rogers, Realising superoscillations: A review of mathematical tools and their application, J. Phys.: Photonics **2**, 042004 (2020).

[35] N. I. Zheludev and G. Yuan, Optical superoscillation technologies beyond the diffraction limit, Nat. Rev. Phys. **4**, 16 (2021).

[36] E. Abbe, Beiträge zur Theorie des Mikroskops und der mikroskopischen Wahrnehmung, Archiv für mikroskopische Anatomie **9**, 413 (1873).

[37] G. Chen, Y. Li, A. Yu, Z. Wen, L. Dai, L. Chen, Z. Zhang, S. Jiang, K. Zhang, and X. Wang, Super-oscillatory focusing of circularly polarized light by ultra-long focal length planar lens based on binary amplitude-phase modulation, Sci. Rep. **6**, 1 (2016).

[38] G. Chen, K. Zhang, A. Yu, X. Wang, Z. Zhang, Y. Li, Z. Wen, C. Li, L. Dai, and S. Jiang, Far-field sub-diffraction focusing lens based on binary amplitude-phase mask for linearly polarized light, Opt. Express **24**, 11002 (2016).

[39] G. H. Yuan, S. Vezzoli, C. Altuzarra, E. T. Rogers, C. Couteau, C. Soci, and N. I. Zheludev, Quantum super-oscillation of a single photon, Light: Sci. Appl. **5**, e16127 (2016).

[40] G. Chen, Z. X. Wu, A. P. Yu, Z. H. Zhang, Z. Q. Wen, K. Zhang, L. R. Dai, S. L. Jiang, Y. Y. Li, L. Chen, *et al.*, Generation of a sub-diffraction hollow ring by shaping an azimuthally polarized wave, Sci. Rep. **6**, 37776 (2016).

[41] W. Zhixiang, J. Qijian, Z. Kun, Z. Zhihai, L. Gaofeng, W. Zhongquan, Y. Anping, and C. Gang, Binary-amplitude modulation based super-oscillatory focusing planar lens for azimuthally polarized wave, Opto-Electron. Eng. **45**, 170660-170661 (2018).

[42] A. P. Yu, G. Chen, Z. H. Zhang, Z. Q. Wen, L. R. Dai, K. Zhang, S. L. Jiang, Z. X. Wu, Y. Y. Li, C. T. Wang, and X.

G. Luo, Creation of sub-diffraction longitudinally polarized spot by focusing radially polarized light with binary phase lens, Sci. Rep. **6**, 38859 (2016).

[43] E. T. F. Rogers, S. Savo, J. Lindberg, T. Roy, M. R. Dennis, and N. I. Zheludev, Super-oscillatory optical needle, Appl. Phys. Lett. **102**, 031108 (2013).

[44] G. Yuan, E. T. Rogers, T. Roy, G. Adamo, Z. Shen, and N. I. Zheludev, Planar super-oscillatory lens for sub-diffraction optical needles at violet wavelengths, Sci. Rep. **4**, 1 (2014).

[45] F. Qin, K. Huang, J. Wu, J. Jiao, X. Luo, C. Qiu, and M. Hong, Shaping a subwavelength needle with ultra-long focal length by focusing azimuthally polarized light, Sci. Rep. **5**, 1 (2015).

[46] G. Chen, Z. Wu, A. Yu, K. Zhang, J. Wu, L. Dai, Z. Wen, Y. He, Z. Zhang, and S. Jiang, Planar binary-phase lens for super-oscillatory optical hollow needles, Sci. Rep. **7**, 1 (2017).

[47] J. Wang, W. Chen, and Q. Zhan, Engineering of high purity ultra-long optical needle field through reversing the electric dipole array radiation, Opt. Express **18**, 21965 (2010).

[48] S. Zhang, H. Chen, Z. Wu, K. Zhang, Y. Li, G. Chen, Z. Zhang, Z. Wen, L. Dai, and A. L. Wang, Synthesis of sub-diffraction quasi-non-diffracting beams by angular spectrum compression, Opt. Express **25**, 27104 (2017).

[49] Z. Wu, K. Zhang, S. Zhang, Q. Jin, Z. Wen, L. Wang, L. Dai, Z. Zhang, H. Chen, G. Liang, *et al.*, Optimization-free approach for generating sub-diffraction quasi-non-diffracting beams, Opt. Express **26**, 16585 (2018).

[50] Y. Hu, S. Fu, H. Yin, Z. Li, Z. Li, and Z. Chen, Subwavelength generation of nondiffracting structured light beams, Optica **7**, 1261 (2020).

[51] T. Zhang, M. Li, H. Ye, and C. Shi, Ultra-long and high uniform optical needle generated with genetic algorithm based multifocal positions optimization, Opt. Commun. **460**, 125178 (2020).

[52] Y. Zhang, H. Liu, H. Cheng, J. Tian, and S. Chen, Multi-dimensional manipulation of wave fields based on artificial microstructures, Opto-Electron. Adv. **3**, 200002 (2020).

[53] B. Born and E. Wolf, *Principles of Optics*, 6th ed. (Pergamon, Oxford, 1993).

[54] J. Gao, S. Yan, Y. Zhou, G. Liang, Z. Zhang, Z. Wen, and G. Chen, Polarization-conversion microscopy for imaging the vectorial polarization distribution in focused light, Optica **8**, 984 (2021).

[55] N. Jin and Y. Rahmat-Samii, Advances in particle swarm optimization for antenna designs: Real-number, binary, single-objective and multiobjective implementations, IEEE Trans. Antennas Propag. **55**, 556 (2007).

[56] J. Lin, H. Zhao, Y. Ma, J. Tan, and P. Jin, New hybrid genetic particle swarm optimization algorithm to design multi-zone binary filter, Opt. Express **24**, 10748 (2016).

[57] See the Supplemental Material at http://link.aps.org/supplemental/10.1103/PhysRevApplied.19.014041 for the experimental procedure and data processing (S1), the effectiveness of a high NA optical microscopy system to measure the superoscillation focusing spot (S2), and the calculation of the Abbe diffraction limit (S3).

[58] F. M. Huang and N. I. Zheludev, Super-Resolution without Evanescent Waves, Nano Lett. **9**, 1249 (2009).

[59] K. S. Rogers, K. N. Bourdakos, G. H. Yuan, S. Mahajan, and E. T. F. Rogers, Optimising superoscillatory spots for far-field super-resolution imaging, Opt. Express **26**, 8095 (2018).

[60] E. T. F. Rogers, J. Lindberg, T. Roy, S. Savo, J. E. Chad, M. R. Dennis, and N. I. Zheludev, A super-oscillatory lens optical microscope for subwavelength imaging, Nat. Mater. **11**, 432 (2012).

[61] F. Qin, K. Huang, J. F. Wu, J. H. Teng, C. W. Qiu, and M. H. Hong, A supercritical lens optical label-free microscopy: Sub-diffraction resolution and ultra-long working distance, Adv. Mater. **29**, 1602721 (2017).